




Dynamical formation of a prethermal Bose-Einstein condensate in a Floquet-engineered latticeJ. Maslek , C. A. Bracamontes, and J. V. Porto *Joint Quantum Institute, NIST/University of Maryland, College Park, Maryland 20742, USA* (Received 19 November 2023; revised 12 April 2024; accepted 15 April 2024; published 3 June 2024)

We experimentally realize an effective Hamiltonian with a continuously adjustable staggered gauge field for weakly interacting bosons in an optical lattice. Periodic driving realizes a staggered Φ -flux model, where Φ can be continuously tuned around π or 2π . We study heating and prethermal relaxation in the modulated lattices following sudden changes in the effective fields. By quenching the system between different Floquet-induced fields with different ground states, we observe Bose recondensation of quench-excited atoms on time scales faster than heating due to the drive. These results are necessary steps towards the generation of correlated states by Hamiltonian modulation, but drive-induced heating (observed here in the weakly interacting limit) is poorly understood in the highly correlated limit and needs to be further studied to determine if such correlated states are realizable.

DOI: [10.1103/PhysRevA.109.063302](https://doi.org/10.1103/PhysRevA.109.063302)**I. INTRODUCTION**

Ultracold atoms in periodically driven quantum systems serve as a highly flexible tool for exploring novel phenomena. In the “Floquet” approach to describing periodically modulated systems, the time-dependent Hamiltonian can often be described by a static, effective Hamiltonian that can exhibit behavior not present in an undriven system. Floquet modulation of ultracold atomic systems has been used to realize conventional and unconventional classical magnetic models [1–5], the Haldane model [6,7], a moatlike dispersion [8,9], anomalous topological states associated with the periodic nature of the Floquet energy structure [10], density-dependent gauge fields [11,12], and the Harper-Hofstadter model [13–16], which can exhibit topologically nontrivial states [6,17].

Much of the interesting physics in Floquet-engineered systems requires interactions. Unfortunately, interacting systems are observed to heat when driven [18–23]. Realising effective Hamiltonians with interactions requires a separation of time scales: the time scale associated with elastic scattering of particles within the Hilbert space described by the effective Hamiltonian should be faster than interaction-induced heating. For lattice systems with bounded spectra, which requires finite local interaction strengths and bounded single-particle spectra, such “Floquet prethermalization” is generally expected in the limit of high-frequency driving [24–27]. While the Hilbert spaces of real systems are not locally bounded, if the states of interest are separated from all other states by a sufficient energy gap, Floquet prethermalization can occur [28].

In lattice systems, the bands of interest are often reasonably isolated, but when considering periodic driving, higher lying bands can be coupled through higher-order resonances, which can result in heating. In the weakly interacting limit, periodically driven, isolated lattice systems have been used to simulate artificial gauge fields [13,17,29–31] and spin-orbit coupling, and engineer interesting band structure [3,7,8]. In

these systems, Floquet prethermalization is not guaranteed and heating depends on specific details of the system. Previous Floquet-engineered experiments using Bose-Einstein condensates (BEC) have relied on the existence of a Floquet prethermal time scale, since the BEC had to be stable long enough to prepare it in a Floquet state [1,4,13,32–38].

Here, we experimentally study thermalization of bosons subject to a Floquet-engineered effective Hamiltonian with a continuously adjustable staggered flux Φ . Starting with a BEC subject to an initial Φ and quenching to a different Φ with a different ground state, we observe recondensation of quench-excited atoms on time scales faster than global heating due to the drive. The resulting (staggered-vortex) state occupies the ground state of the *effective* Hamiltonian. We note that this state can also be created with a non-Floquet approach, by exciting atoms to higher bands in static optical lattices [39,40]. Interestingly, similar recondensation is observed in the non-Floquet approach, except that decay from the excited band limits the long-time behavior, instead of drive-induced heating.

We explore two effective field configurations: a staggered 2π regime with topologically trivial band structure related to the field-free state by a gauge transformation and a nontrivial staggered Φ -flux model with $\Phi \simeq \pi$ [13], where near $\Phi = \pi$ the single-particle band structure displays minima at two inequivalent points in the lowest Brillouin zone (BZ). (Note that while gauge-independent observables are completely insensitive to a 2π gauge transformation, for the artificial gauge field used here, the system observables are gauge dependent.) The latter system is expected to exhibit a phase transition for interacting bosons when tuning Φ across $\Phi = \pi$ [41–43].

In both field configurations, when the gauge-field quench is applied to a BEC, the resulting sudden shift of the quasimomentum of the equilibrium ground state leads to fast heating followed by recondensation at the new band minima of the effective Hamiltonian of the driven system. Such postquench relaxation was recently proposed as an efficient mechanism for preparation of Floquet-engineered states in a Hofstadter

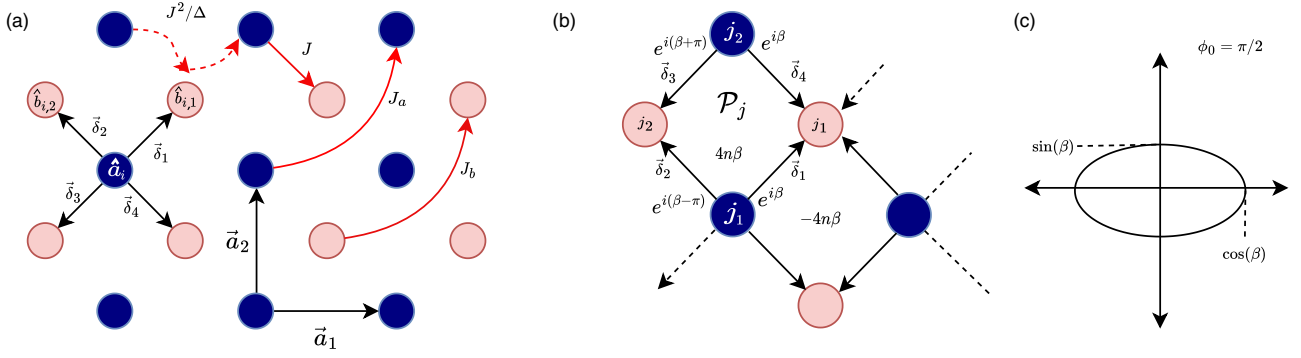


FIG. 1. Schematic of the real-space lattice geometry. (a) The two sublattices [A (blue) and B (red)] are offset in energy by $\hbar\Delta$. The principle lattice vectors are \mathbf{a}_1 and \mathbf{a}_2 , where $|\mathbf{a}_\alpha| = \lambda/\sqrt{2}$. (λ is the wavelength of the lattice beams.) The reciprocal lattice vectors, defined by $\mathbf{a}_\alpha \cdot \mathbf{b}_\beta = 2\pi\delta_{\alpha\beta}$, have magnitude $|\mathbf{b}_\alpha| \equiv k_L$, where $k_L = \sqrt{2}k_R$ and $k_R = 2\pi/\lambda$. The A sites of the lattice have creation-annihilation operators a_i^\dagger/a_i , where \mathbf{i} is a two-dimensional index spanning the lattice. The four nearest neighbors of each A site living on the B sublattice have associated operators $b_{i,\mu}^\dagger/b_{i,\mu}$ ($\mu = \{1, 2, 3, 4\}$). The relative position between the i th A site and the four $\{i, \mu\}$ B sites are $d\hat{\delta}_\mu$, where $d = \lambda/2$. The angles between the x axis and $\hat{\delta}_\mu$ are $\phi_\mu = \pi/4, 3\pi/4, 5\pi/4, 7\pi/4$. Static tunneling processes up to order J^2 are indicated: (1) nearest-neighbor coupling with strength J , which is suppressed by the offset Δ ; (2) resonant second-order tunneling to next-nearest neighbors on the same sublattice, which scale as $\sim J^2/\Delta$; (3) direct next-nearest-neighbor tunneling processes (inherent to the static lattice) with strengths J_a and J_b that scale as $\sim J^2/E_R$. (b) Effective gauge field model: periodic drive restores tunneling between sublattices, with complex tunnel coefficients $\mathcal{J}_n(\alpha A_\mu)e^{-in\phi_\mu}$ along $\hat{\delta}_\mu$ (see Appendix A 1). The phase factors acquired when traversing a plaquette clockwise, including the sign associated with the tunneling direction relative to $\hat{\delta}_\mu$, are indicated. Near-resonant driving, $\Delta \simeq n\omega$, results in an effective two band system that exhibits a staggered- $n\pi$ flux. (c) Elliptical drive trajectory shown for a fixed $\phi_0 = \pi/2$.

band [44]. Finally, using the ability to continuously change the staggered flux around π , we observe relaxation between the two inequivalent minima of the π flux model.

II. STAGGERED FLUX MODEL

A. Ideal tight-binding model

We consider bosons on a 2D checkerboard lattice subject to a time-periodic elliptical displacement of the lattice with period T (Fig. 1). The lowest-order effective Hamiltonian for this system is a two-band, tight-binding staggered Φ -flux model, where $\beta = \Phi/4$ is a continuous, variable phase picked up when tunneling along one leg of a square plaquette in the lattice (see Appendix A 1). As we will emphasize below, an accurate model requires inclusion of higher-order coupling to additional bands beyond this low-order tight-binding picture, but we start by considering this simple model. Written in terms of the “spoke” numbering (see Fig. 1), the simple effective Hamiltonian for the driven system has the form

$$H = -J \sum_{\mathbf{i}} (e^{in\beta} a_{\mathbf{i}}^\dagger b_{i,1} + e^{-i(n\beta-\pi)} a_{\mathbf{i}}^\dagger b_{i,2} + e^{i(n\beta+\pi)} a_{\mathbf{i}}^\dagger b_{i,3} + e^{-in\beta} a_{\mathbf{i}}^\dagger b_{i,4} + \text{H.c.}) - \delta_n a_{\mathbf{i}}^\dagger a_{\mathbf{i}}, \quad (1)$$

where J is the nearest-neighbor tunneling matrix element, Δ is the staggered offset, and $\delta_n = \Delta - n\omega$ is the (small) detuning from the n th-order resonance, \mathbf{i} is a two-dimensional index spanning the lattice, and $b_{i,\mu}$, $\mu = \{1, 2, 3, 4\}$, act on the four B sites tunnel coupled to the site $a_{\mathbf{i}}$ along directions $\hat{\delta}_\mu$. Here, we consider $n = 1$ ($\omega \simeq \Delta$) and $n = 2$ ($\omega \simeq \Delta/2$). Given the geometry of neighboring plaquettes, the flux pattern is staggered, since tunneling in an opposite direction is associated with complex conjugation, negating the acquired phase.

In momentum space, the ideal case band structure for Eq. (1) with $\delta_n = 0$ is given by [29]

$$\epsilon_{\pm} = \pm J \mathcal{J}_n(\alpha) |G_n(\mathbf{q})|, \quad (2)$$

where \mathcal{J}_n is the n th-order Bessel function, α is the normalized drive strength (proportional to the magnitude of the driving force), and $G_n(\mathbf{q})$ are \mathbf{q} -dependent functions that arise in the tight-binding calculation of the Floquet effective Hamiltonian (see Appendix A 1.) The band structure depends on the order n of the resonance: a staggered- 2π case has a single minimum at the point $q_{\min} = \mathbf{M} = \frac{1}{2}(\pm\mathbf{b}_1 \pm \mathbf{b}_2)$; see Fig. 2(a). This band is equivalent to the zero flux case, Fig. 2(e), up to a gauge transformation that translates $\mathbf{q}' \rightarrow \mathbf{q} + \frac{1}{2}(\pm\mathbf{b}_1 \pm \mathbf{b}_2)$. While the low-energy physics confined to the driven lattice is gauge independent [45], the underlying gauge is experimentally accessible for synthetic magnetic fields and the gauge has physical significance for measurements that access high-energy states, such as suddenly turning off the lattice to project the state onto the free particle basis. In particular, a sudden shift in the band minimum from $\mathbf{q} = (0, 0) \equiv \mathbf{\Gamma}$ to point \mathbf{M} will cause heating and require rethermalization to relax to the new, shifted ground state. Additionally, the physical gauge is observable in time-of-flight momentum measurements after projecting onto free particle states by suddenly turning off the drive.

For the staggered- π case, the ground band has two minima at inequivalent points in the BZ of the staggered lattice defined by $\mathbf{b}_{1,2}$ [see Fig. 2(c)], which are degenerate at $\Phi = \pi$. (The staggered lattice BZ is $1/\sqrt{2}$ smaller and rotated by $\pi/4$ relative to the BZ associated with square, unstaggered lattice of spacing $d = \lambda/2$. The square lattice BZ corresponds to the *second* BZ of the staggered lattice.) The twofold degeneracy persists in the presence of interactions and is indicative of nonzero (staggered) π flux [13,42,46]. We note that, in

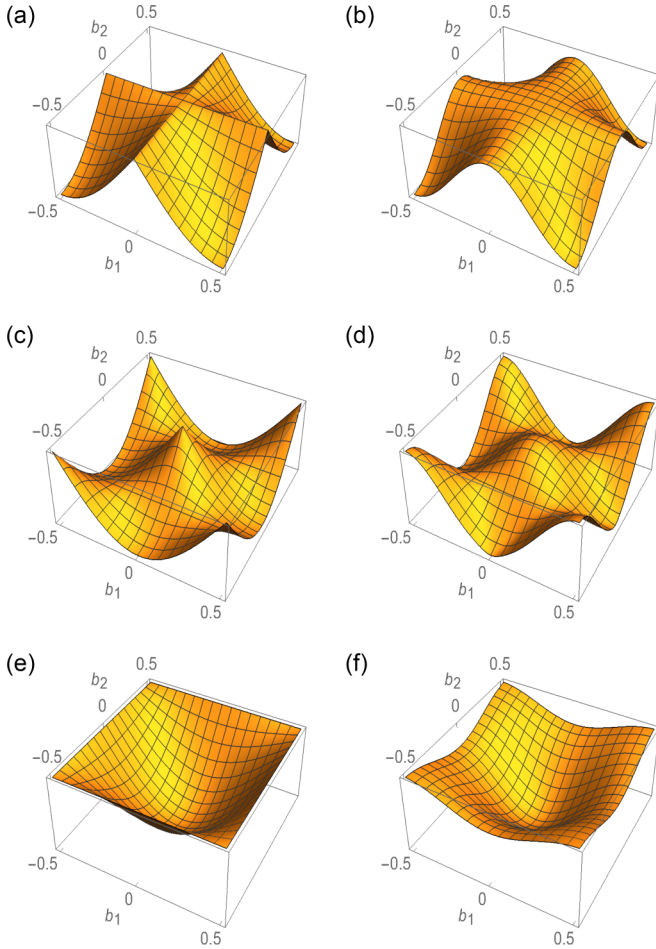


FIG. 2. Effective Floquet band structure. Left column: lowest-order tight-binding Floquet band structure for $n\pi$ staggered flux; right column: more accurate Floquet band structure, under the same conditions as the left column. The extended calculations include contributions at second order in tunneling, $\propto J^2$, as well as effects from higher bands. (a), (b) The 2π case has a single ground-state minimum at point \mathbf{M} in the BZ, which, due to the periodic boundary conditions, occurs at the equivalent point $\mathbf{q} = \frac{1}{2}(\pm\mathbf{b}_1 \pm \mathbf{b}_2)$. The 2π band structure is simply related to the 0π case shown in (e), (f) by a gauge transformation $\mathbf{q}' \rightarrow \mathbf{q} + \frac{1}{2}(\pm\mathbf{b}_1 \pm \mathbf{b}_2)$. (c), (d) The π -staggered flux case has two inequivalent ground-state minima at \mathbf{X}_+ and \mathbf{X}_- . In addition, the periodicity of the band doubles.

the tight-binding limit, the staggered- π flux is identical to the uniform- π flux, which realizes a fully frustrated Bose-Hubbard model [13,41,42]. In the gauge appropriate for our experimental realization, the minima occur at $q_{\min+} \equiv \mathbf{X}_+ = \pm\frac{1}{2}\mathbf{b}_1$ and $q_{\min-} \equiv \mathbf{X}_- = \pm\frac{1}{2}\mathbf{b}_2$. When $\delta_1 = 0$, there are two inequivalent Dirac points (\mathbf{q}_{D_i} , $i = \{1, 2\}$), at which the gap to the second band (not shown in Fig. 2) closes linearly with $|\mathbf{q} - \mathbf{q}_{D_i}|$. In the ideal case [Fig. 2(c)] both gaps close at $\delta_1 = 0$. With the more realistic model described below [Fig. 2(d)], the Dirac points occur at different δ_1 and a topological regime occurs for a (small) range of parameters between the gap closings [29].

The experimental focus of this paper is to study dynamics following quenches between these effective field configurations, which have different band minima.

B. Realistic lattice model

The dispersion given by Eq. (2) is only the lowest-order approximation to the real driven lattice. There are several important corrections missing from this model. First, the Floquet treatment of Eq. (A 1) has higher-order corrections that should be included to accurately describe the band structure. Taking the high-frequency Floquet expansion to order (J^2/ω) gives rise to additional α -dependent terms that are second order in the hopping. We note that although the lowest-order dispersion, Eq. (2), vanishes in the limit that the drive strength goes to zero, $\alpha \rightarrow 0$, the $J^2/\omega \simeq nJ^2/\Delta$ terms are nonzero at $\alpha = 0$. In particular, the lowest-order terms in α and J scale as $\mathcal{J}_1(\alpha)J + \mathcal{J}_0(\alpha)J^2/\omega \simeq \alpha J + nJ^2/\Delta$. These second-order hopping terms are dominant at small α and must be included.

To be consistent, if we include Floquet terms to second order in J , we should include the two-site hopping J_{ij} which also scale as J^2 . This hopping is a direct process inherent to the static lattice, whereby an atom tunnels two sites to the next-nearest sites; see Fig. 1. These terms are small, but nonzero, even in the case of a simple $\Delta = 0$ square lattice. Normally ignored, they are the same order of magnitude as the second-order Floquet hopping. Including both the higher-order Floquet and two-site hopping terms gives a two-band tight-binding dispersion $\epsilon_{\pm}(\mathbf{q}) = \epsilon_{\pm}(\mathbf{q}, \alpha, \omega, \delta_n, J, J_a, J_b)$ that, in addition to J and ω , depends on α , δ_n , and the two-site hopping parameters J_a and J_b . The full expression for ϵ_{\pm} is given in Appendix A 1 and several examples are shown in Fig. 2.

The two-band tight-binding approximation including two-site hopping does a good job of capturing the overall shape of the Floquet bands at small drives. However, this model breaks down at higher values of α , as a result of coupling to higher bands not present in the two-band description. A full treatment of the system can be performed in the extended basis, which considers a larger number of lattice bands; see Appendix A 2. The coupling to higher bands results in several effects. First, off-resonant coupling to higher bands modifies the effective tight-binding parameters, which must be accounted for in order to correctly determine the parameters. In addition, the coupling to higher bands breaks the symmetry between the A and B sites: the B sites, which by definition are higher in energy [Eq. (1)], are more strongly coupled to the excited bands, which leads to larger micromotion, for example. More consequentially, resonant n -photon coupling gives rise to dramatic shifts in the band shapes and direct excitation to higher bands, making it challenging to adiabatically navigate through parameter space, particularly near the resonant π -flux case, $\Delta \simeq \omega$.

These effects can be seen in Fig. 3, which shows the extended basis calculation of the Floquet quasienergies as a function of drive frequency, ω , at $\mathbf{q} = [\Gamma, \mathbf{M}, \mathbf{X}_{\pm}]$, the three different points within the BZ where the bands exhibit minima. Figure 3(a) shows the lowest quasienergies in the full extended system, where the boxes indicate the regions near the ω , 2ω resonance conditions that are plotted in Fig. 3(b) and Fig. 3(c). Zooming into the $n = 1$ resonance, Fig. 3(b), one can see that the frequency at which the two bands cross at $\mathbf{q} = \Gamma$ (black lines) is no longer equal to the $\alpha = 0$ resonance condition (green dashed line), indicating a shift in

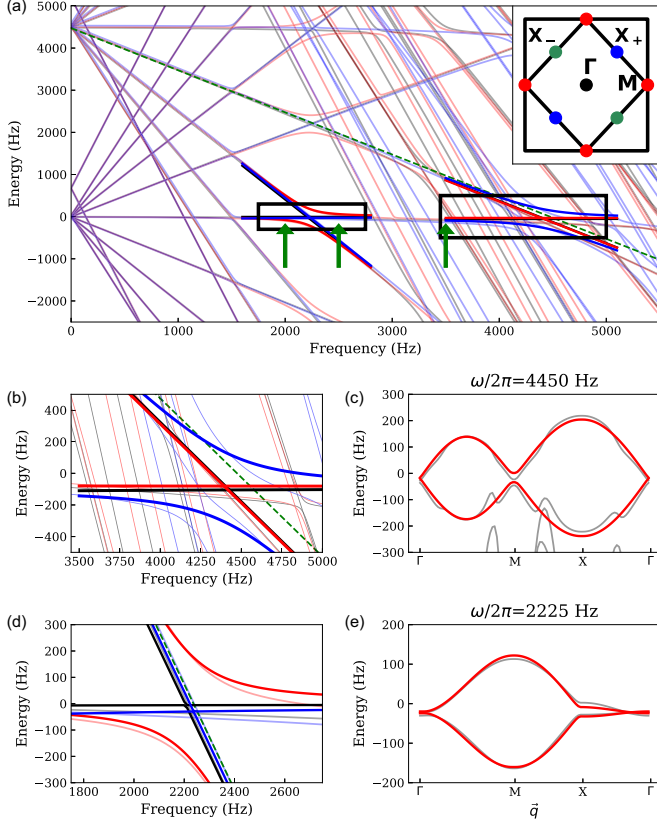


FIG. 3. Extended basis calculation of the Floquet quasienergy spectrum vs drive frequency $\omega/2\pi$, shown for $\mathbf{q} = \Gamma$ (black), $\mathbf{q} = \mathbf{M}$ (red), and $\mathbf{q} = \mathbf{X}$ (blue) at $\alpha = 2.0$; see Appendix A 2. Thin transparent lines indicate the extended basis calculation and thick solid lines indicate a tight-binding fit. The inset in (a) shows the lowest two BZs of the staggered lattice, where the labeled points match the lines shown in (a), (d), and (e). Panels (b) and (d) show the spectra zoomed into the black rectangular regions in (a). The green dashed lines indicate the line $\Delta - \omega$. Panels (c) and (e) show the resulting bands along the symmetry line (Γ - \mathbf{M} - \mathbf{X} - Γ) at a fixed frequency for the full matrix calculation (black) and the tight-binding approximation (red). The green arrows in (a) indicate the load conditions in Fig. 4.

the tight-binding δ_1 . In addition, avoided band crossings are evident for all three \mathbf{q} in the BZ. Figure 3(c) shows the band structure calculated near resonance (black curve) as well as the tight-binding fit (red curve). We find that there are many higher-order avoided-crossing couplings for the $n = 1$ resonance, which result in significant heating when loading the condensate into the Floquet lattice. There are regions in parameter space below resonance, however, that do not have strong higher band coupling and yet still have band minima at the staggered π -flux condition $\mathbf{q} = \mathbf{X}_{\pm}$. These regions that produce well-isolated bands with minimal coupling are explored in Fig. 4.

III. EXPERIMENT

Our experiment begins with a ^{87}Rb BEC of approximately 3×10^4 atoms in the $|F = 1, m_F = -1\rangle$ state held in a crossed optical dipole trap. A 2D checkerboard lattice [47,48] with $\lambda = 813$ nm was adiabatically turned on

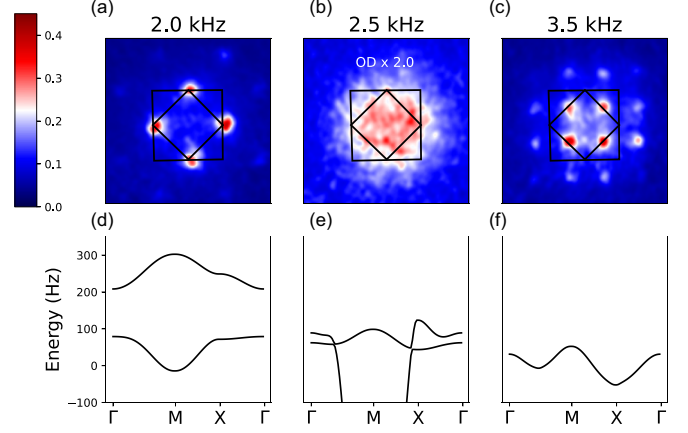


FIG. 4. Adiabatic loading of Floquet states. (a)–(c) Micro-motion-averaged time-of-flight images of condensates loaded adiabatically into the Floquet lattice at different drive frequencies (see Appendix A 1). The first two BZs are indicated with black lines. In all cases, the states were prepared by ramping on the shaking in 12 ms at fixed frequency to a final drive strength $\alpha = 2$. The frequencies are (a) $\omega/2\pi = 2.0$ kHz $\lesssim \Delta/2$, (b) $\omega/2\pi = 2.5$ kHz $\simeq \Delta/2$, and (c) $\Delta/2 < \omega/2\pi = 3.5$ kHz $< \Delta$. The given frequencies are indicated in Fig. 3(a) by the green arrows. For $\omega/2\pi = 2.0$ kHz $\lesssim \Delta/2$, corresponding to a staggered 2π effective B field, the BEC condenses at the single equivalent point, $\mathbf{M} = \{\pm\mathbf{b}_1, \pm\mathbf{b}_2\}$. For $\Delta/2 < \omega/2\pi < \Delta$, corresponding to staggered- π flux, the BEC condenses at the two inequivalent points $\mathbf{X}_{\pm} = \{0, \pm\mathbf{b}_1\}$ and $\mathbf{X}_{\pm} = \{\pm\mathbf{b}_1, 0\}$. (d)–(f) Calculated band structure along the path Γ - \mathbf{M} - \mathbf{X}_{\pm} - Γ of the two lowest bands for the conditions in (a) and (b).

in 200 ms to the target depth, with a variable offset between neighboring sites. In our lattice, $E_R = \hbar^2 k_R^2 / 2m = h \times 3.5$ kHz is the single-photon recoil energy and $k_R = 2\pi/\lambda$ is the single-photon wave vector (m is the mass of ^{87}Rb). We used lattice depths of $\simeq 7 E_R/h$ ($= 24.5$ kHz) and staggered offsets $\Delta/h \simeq 4$ kHz to 5 kHz, for which the nearest-neighbor tunneling strength is $J \simeq h \times 120$ Hz and the on-site interaction energy at the center of the trap is approximately $U \simeq h \times 550$ Hz. Two piezoactuated mirrors [49] allow us to translate the lattice along an elliptical trajectory with an amplitude ($\lesssim 3$ μm) and frequency ($\lesssim 20$ kHz): $\mathbf{r}(t) = \{\Delta x \sin(\omega t - \phi), \Delta y \cos(\omega t - \phi)\}$. As we discuss below, the ellipticity of the trajectory determines the magnitude of the staggered field. We adjust the phase of the drive relative to the time origin of the experiment in order to measure and mitigate micromotion effects.

A. Adiabatic loading

We first observe the condensation at finite momentum for different effective flux patterns resulting from circular drive. Starting with a BEC loaded at $\mathbf{q} = 0$, we ramp on the drive at a fixed frequency in 12 ms to a final drive strength α . The 12 ms turn on time was chosen to be long enough that there was thermalization and no projection to higher bands and short enough that there was minimal drive-induced heating out of the condensate. Once the ramp is completed, the drive is abruptly stopped and all confining potentials are turned off.

We measure the momentum distribution through absorption imaging after a 29 ms time of flight (TOF).

Figure 4 shows the condensate after a linear ramp of the drive strength to $\alpha = 2$ for three different frequencies. Measurements were taken for circular drive ($\beta = \pi/4$) in a $7.2 E_R$ total final lattice depth, with a $\mathbf{q} = 0$ gap between the two lowest bands equal to $\hbar \times 4.7$ kHz. The presented images are an average over individual images taken at different drive phases, in order to average over the micromotion.

The distinct change in the condensation quasimomentum at different circular drive frequencies results from the discrete change in effective flux from 2π to π . Below the $n = 2$ resonance, the cloud relaxes into a condensate at the *single* minimum associated with the staggered 2π flux in our system. This can be seen in the TOF image in Fig. 4(a), where the condensate in the single minimum is projected onto the four free particle momenta $\frac{1}{2}(\pm\mathbf{b}_1 \pm \mathbf{b}_2)$ before the TOF measurement.

Below the $n = 1$ resonance, we observed condensation at the two inequivalent minima associated with the staggered π flux at \mathbf{X}_+ and \mathbf{X}_- , as shown in Fig. 4(c). The noninteracting single-particle states at the band minima, ψ_+ and ψ_- , are degenerate and any superposition of them breaks the translational symmetry of the Hamiltonian [42]. We discuss these degenerate band minima and the phase transitions expected when varying the system between ground states preferring one of the two minima below.

At intermediate driving frequency the atoms fill the band, which coincides with the regime where the band's minimum at $\mathbf{q} = \Gamma$ becomes energetically equal to the two-band minima at $\mathbf{q} = \mathbf{X}_{\pm}$ resulting in a flatter band. In addition, there are intersecting higher bands that can cause heating [see Fig. 4(e)].

For the ideal case band structure [Eq. (2)], the band minima associated with the staggered flux appear for any nonzero drive α . As noted above, at small α the second-order terms are dominant and one needs a sufficient drive to make the flux terms dominant. At a given frequency, the band minimum will therefore depend on the drive strength. For the 2π staggered flux, which has an ideal-case minimum at \mathbf{M} , there is a region in low α where $E(\Gamma) < E(\mathbf{M})$. We observe this change in minima with drive frequency in Fig. 5, where we adiabatically load at $\omega = 2$ kHz to a given drive α in 12 ms and measure a visibility between the populations at $\mathbf{q} = \Gamma$ and $\mathbf{q} = \mathbf{M}$. We find the visibility between the \mathbf{q} points varies with α as the calculated energy difference of the two minimum switches sign.

B. Tuning across $\Phi = \pi$

Cold-atom systems with two or more degenerate dispersion minima have been studied in 1D [4] and 2D [1,2,13,39,40,45,50,51] lattice systems. For weakly interacting Bose particles, a magneticlike phase transition is expected when varying system parameters such that the dispersion degeneracy is crossed [42,43]. The nature of the transition depends on whether the two phases on either side of $\Phi = \pi$ are miscible or tend to phase separate [4,45]. Tuning the effective interactions from repulsive to attractive changes the nature of the phase transition from a \mathbb{Z}_2 transition with a phase separated state at the transition to one in which the magnetic

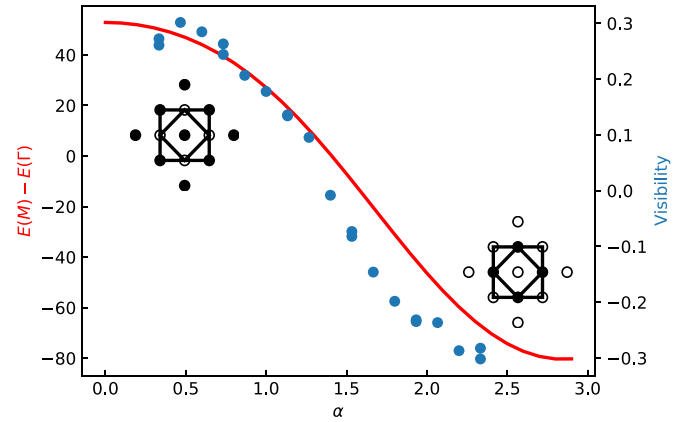


FIG. 5. Visibility between $\mathbf{q} = \Gamma$ and $\mathbf{q} = \mathbf{M}$ for condensates loaded into the Floquet bands at a final α , for a drive frequency below the $n = 2$ resonance. The blue points represent the measured visibility between the two q points, $V = (N_{\Gamma} - N_{\mathbf{M}})/(N_{\Gamma} + N_{\mathbf{M}})$. The red curve indicates the energy difference, $E(\mathbf{M}) - E(\Gamma)$ vs α , obtained through the extended basis calculations, showing that the inversion of band minima is dependent on both ω and the drive strength.

states are separated by a miscible phase with second-order transitions to the magnetic phases [45].

In 2D spin-orbit coupled experiments without a lattice [52], for example, the single-particle Hamiltonian was tuned between two regimes with distinct single band minima, with a transition between the regimes occurring when the two minima were degenerate. The direct observation of the phase transition associated with crossing the band degeneracy was challenging in this case due to the effective conservation of magnetization in cold atom systems, which resulted in long-lived metastable states that did not relax toward the magnetic ground state. (Exactly at the degeneracy point, however, a miscible to immiscible phase transition was observed, which results from the tuning of the effective dressed interactions as spin-orbit coupling was turned on.)

Considering only single-particle states at the degenerate band minima for the single effective band model, the state space consists of two states, which we label ψ_+ and ψ_- . If interactions are weak and do not significantly couple to other states [42,43], the continuum of possible superposition states can be written

$$\psi(\sigma, \xi) = \cos \sigma \psi_+ + \sin \sigma e^{i\xi} \psi_- . \quad (3)$$

The \mathbb{Z}_2 nature of the transition for repulsive interactions means that of the continuum of states, $\psi(\sigma, \xi)$, two of these ground states remain degenerate, ψ_{\uparrow} and ψ_{\downarrow} . It was argued in [41] that for a continuously variable flux Φ , the transition point $\Phi = \pi$ is a first-order phase transition. One expects large fluctuations in the measured populations $|\psi_{\uparrow}|^2$ and $|\psi_{\downarrow}|^2$ for systems prepared at the degenerate condition $\Phi = \pi$. Such large fluctuations were seen in both 1D [4] and 2D [1] double-well dispersion systems. Depending on the physical gauge in which the dispersion is realized, however, the observable accessible by projecting the gauge-dressed state onto free particle states (measured in TOF) may not be sensitive to the difference between $|\psi_{\uparrow}|^2$ and $|\psi_{\downarrow}|^2$. Such insensitivity to the difference of the two states was described in [42] and

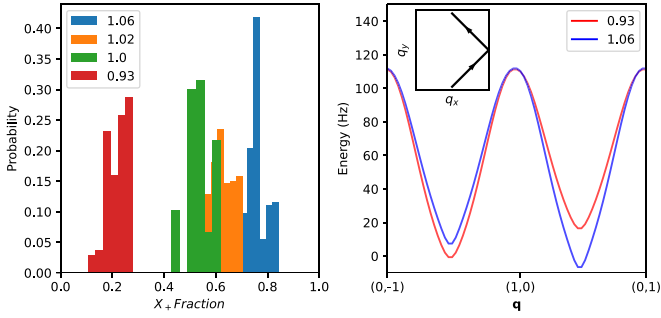


FIG. 6. Left panel: histogram of the fraction of the total population in X_+ for different flux configurations across the $\Phi = \pi$ boundary. Right panel: extended basis calculation of the energy along a path containing the two minima at X_+ and X_- , for the two extreme fluxes shown in the left panel. The total single-particle energy difference between the ground state and the nonequilibrium initially prepared state is ≈ 10 Hz. The inset indicates the path chosen for the cross sections, showing the imbalance between the two configurations, where the square indicates the boundary of the second BZ.

experimentally confirmed in [50] for the Landau-like gauge. (See Appendix B for a discussion of the differences between the gauge used in Ref. [42] and the gauge we employ here.)

In our physical gauge, $\psi_\uparrow = \psi_+$ and $\psi_\downarrow = \psi_-$ project onto distinct plane-wave components, giving rise to distinguishable expansion images. Based on the effective Floquet Hamiltonians described above (either the tight-binding model or the extended basis model) one would expect to see significant fluctuations of the measured populations $|\psi|^2$ between $|\psi_+|^2$ and $|\psi_-|^2$ for $\Phi = \pi$.

In order to study the fluctuations near $\Phi = \pi$, we prepare the condensate by ramping on the drive, as in Fig. 4(c), but with a small, adjustable ellipticity in the trajectory (close to circular). We control the effective gauge field by adjusting the relative amplitudes of our two piezomirrors, which shifts the trajectory from a strictly circular displacement and breaks the symmetry between the X_\pm points (see Appendix A 1). We measured the relative populations after adiabatically loading the atoms into the $\simeq \pi$ -flux lattice at different ellipticities.

In Fig. 6, we show the distribution of relative X_+/X_- populations for different fluxes. The data was obtained by measuring the populations after an adiabatic turn on of the drive and a sudden quench back to the static bands. We find that, contrary to the expectation based on the effective Floquet model (see Appendix B), the condensate consistently relaxed into a state with well-defined relative population of X_+ and X_- , with small fluctuations around the measured ratio. This lack of fluctuations indicates that either some perturbation not included in the model selects for equal populations in the two minima or that thermal effects destroy the “spontaneous symmetry breaking.” Both explanations are plausible, since the single-particle energy scale differentiating X_+ and X_- is quite small, indicating that interactions dominate the behavior of the system. We observe that breaking the degeneracy by only ± 10 Hz shifts the mean population balance significantly [see Fig. 6(b)]. In addition, while it is hard to determine (or even define) an effective temperature in our short-lived

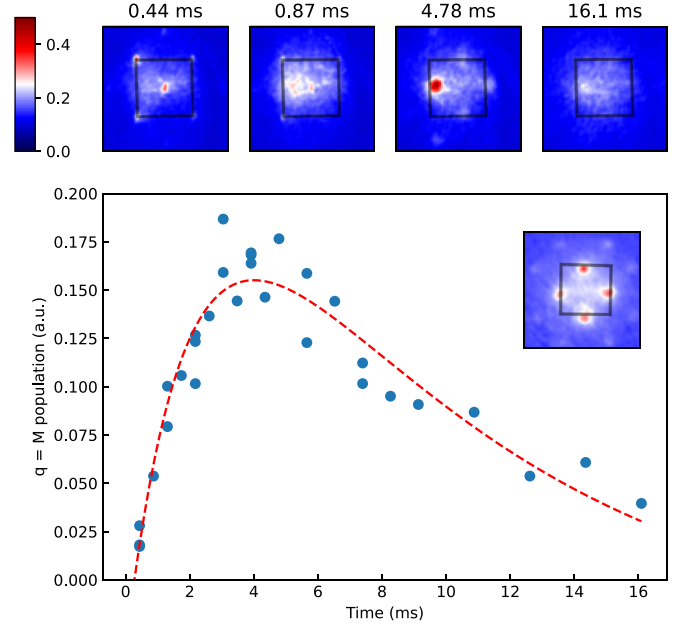


FIG. 7. BEC relaxation dynamics between the 0-flux and the 2π -flux configurations, at $\omega/2\pi = 2.3$ kHz. After quenching on the drive, the BEC, initially at $\mathbf{q} = \Gamma$, quickly relaxes into $\mathbf{q} = M$. The plot shows the population in the $\mathbf{q} = M$ state (see Appendix C). The data was taken at a fixed end phase. For reference, the inset shows a phase-averaged image of the cloud when adiabatically loaded into the final 2π flux Floquet lattice. The dashed line is a fit to a two exponential relaxation, with an initial fast relaxation time of 2.1 ms and a longer decay time of 9.1 ms, where the longer time scale is also associated with atom loss. The boundary of the second BZ is indicated by the black lines in the representative fixed-phase absorption images.

Floquet system, higher temperatures are expected to destroy the spontaneous magnetization [2].

C. Prethermal relaxation

To observe the relaxation dynamics, we project the undriven state of the condensate onto the Floquet basis Hamiltonian by abruptly turning on the drive. To ensure that we only populate states that are adiabatically connected to the undriven ground band, we ramp on the drive over a single period, T , which minimizes excitation to higher bands. The drive is then held for an integer number of periods, after which the lattice is snapped off (in $\lesssim 2 \mu\text{s}$). Figure 7 shows the relaxation dynamics as a function of hold time after abruptly turning on the lattice, for the $n = 2$ case, with $\omega/2\pi = 2.3$ kHz and $\alpha = 2$. Starting with a condensate at $\mathbf{q} = \Gamma$, we see fast decay of the condensate followed by recondensation at the $\mathbf{q} = M$ band minimum, on a time scale of $\simeq 2$ ms. This time scale is faster than the $\simeq 10$ ms time scale of heating-induced loss of population given by the second time constant determined in the fit in Fig. 7. Interestingly, these time scales are comparable to those observed in a similar band structure that was created using a different, undriven approach where atoms were prepared in higher bands of a static lattice [51].

In the near-resonant case of $n = 1$, significant heating is observed and a single period quench near resonance results in

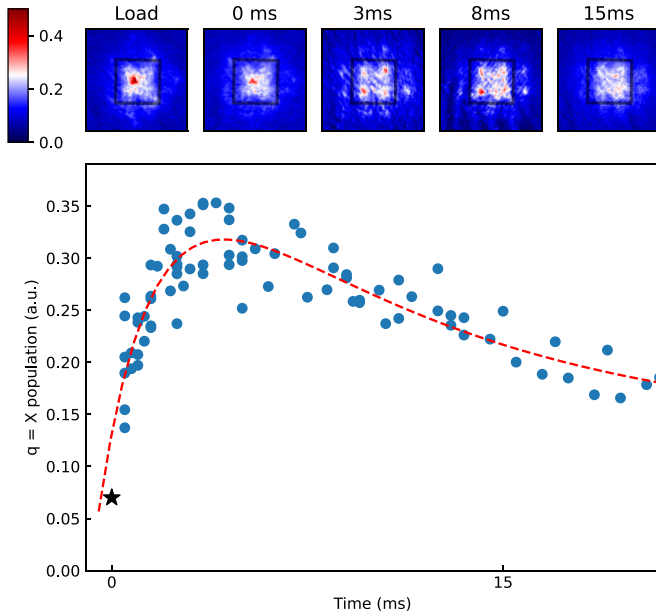


FIG. 8. BEC relaxation dynamics between the 0 flux and the π flux configurations, at $\omega/2\pi = 4$ kHz, using the procedure described in the text. We observe that the BEC initially at $\mathbf{q} = \mathbf{\Gamma}$ quickly relaxes into $\mathbf{q} = \mathbf{X}_{\pm}$. The plot shows a measure of the population in the $\mathbf{q} = \mathbf{X}_{\pm}$ state (see Appendix C) and the star indicates the $\mathbf{q} = \mathbf{X}_{\pm}$ population of the state prior to the quench. The data was taken for fixed end phase. The dashed line is a fit to a two exponential relaxation, with an initial fast relaxation time of 2.1 ms and a longer decay time of 10.6 ms, where the longer time scale is also associated with atom loss. The boundary of the second BZ is indicated by the black lines in the representative phase-averaged absorption images.

a thermal cloud that fails to relax into the new band minima. To mitigate the heating during the quench from $\mathbf{q}_{\min} = \mathbf{\Gamma}$ to $\mathbf{q}_{\min} = \mathbf{X}$, we initially ramped up the drive to $\alpha = 2$ over a period of 3 ms at a higher detuning of $\omega = 3.5$ kHz, where the heating was less severe. We then swept the frequency to 4 kHz in 250 μ s to quench to the near resonance condition. The relaxation dynamics for these conditions are shown in Fig. 8, where the insets show sample images that are phase averaged to display all four minima. We observe relaxation into $\mathbf{q}_{\min} = \mathbf{X}$ on similar time scales as the $\mathbf{q}_{\min} = \mathbf{M}$ case. Remarkably, despite the high drive strengths, where one might expect strong heating, we find the condensate relaxes to the time-dependent Floquet eigenstate corresponding to the effective Hamiltonian ground state.

As previously discussed, the symmetry of the drive can be broken by shaking the lattice along an elliptical trajectory, removing the degeneracy of the bands at $\mathbf{q} = \mathbf{X}_{\pm}$. We study the relaxation dynamics of atoms loaded into ψ_{+} at \mathbf{X}_{+} while driving at one ellipticity and suddenly changing the drive to a different ellipticity for which the minimum state ψ_{-} is at \mathbf{X}_{-} . This results in a small change in effective flux Φ , resulting in a small difference in the band structure at \mathbf{X}_{\pm} : we calculate (using the full extended basis) that the single-particle energy difference between the two configurations is $\lesssim 10$ Hz.

We observe relaxation between minima by loading atoms into one configuration's minimum and then quenching to the other X point's minimum. The resulting prethermal relaxation

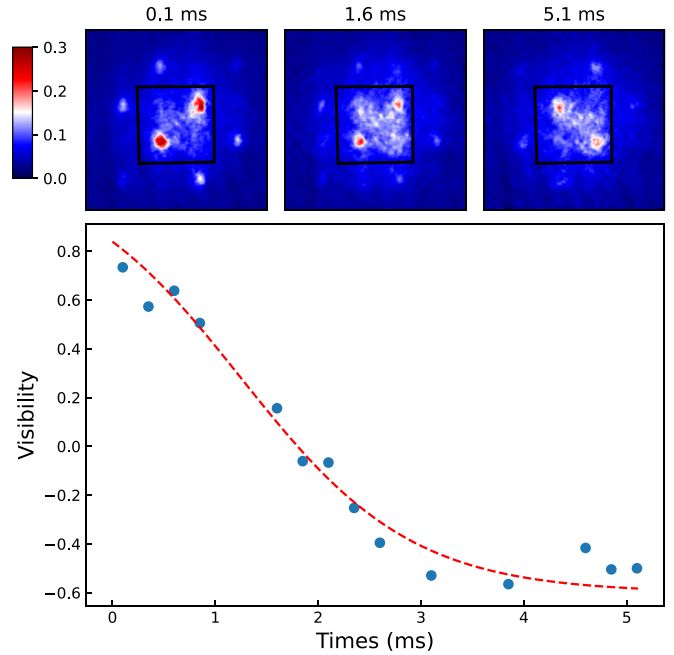


FIG. 9. Relaxation dynamics between band minima after a sudden, small change in the ellipticity of the drive, at a drive strength of $\alpha = 1.5$ and $\omega/2\pi = 4$ kHz. The shaking is ramped on such that the atoms condense into one minima. The drive is then quenched such that the opposite point has lower energy. We measure the relative visibility between the two points as a function of time after the quench and note the relaxation from one to the other. The boundary of the second BZ is indicated by the black lines in the representative phase-averaged absorption images.

is shown in Fig. 9, where we observe relaxation to the new condensation point on a short time scale, similar to the 2 ms observed for the other $n\pi$ quenches shown in Fig. 7. This time scale is consistent with the interaction energy driving the recondensation shown in Figs. 7 and 8, but much faster than the time scale associated with the <10 Hz single-particle energy difference between the two configurations (see Fig. 6). We also note that the relaxation is much faster than in magnetization-conserving spin-orbit coupled systems.

IV. CONCLUSION

In this work, we Floquet engineered an effective Hamiltonian with an adjustable staggered gauge field, which we tune near $n\pi$ for $n = 1$ and $n = 2$. The gauge field arises in the lowest-order tight-binding Hamiltonian describing the system, although the lowest-order Hamiltonian is inadequate to describe the parameter regimes that avoid heating. A tight-binding model that includes higher-order tunneling processes is more accurate, but capturing the possible heating due to resonances requires a full extended-basis Floquet calculation. By using these more realistic models, we identified parameters where an effective gauge field is realized and we experimentally observe interaction-induced equilibration to be faster than the Floquet-induced heating. Thermalization and recondensation of atoms into the gauge-dependent low-energy states was studied, as well as the fluctuations of populations loaded under different flux conditions. Our results

indicate that relaxation within the interacting Floquet basis for our system is possible. It is not clear if the temperatures and densities can be made low enough to realize the highly correlated states expected in this system, but our observations of relaxation from highly nonequilibrium states represent an important step towards using Floquet engineering to realize highly correlated states.

ACKNOWLEDGMENT

We thank I. Spielman for a critical and helpful reading of this paper.

APPENDIX A: FLOQUET TREATMENT OF OPTICAL LATTICES

In the Floquet treatment of periodically driven systems, the quasienergy spectrum exhibits a Brillouin zone–like structure [53], where pseudoenergies ϵ_n are defined up to modulo the drive frequency, $\omega = 2\pi/T$. This energy folding results in a large number of (time-dependent) Floquet states within a given range of ϵ_n . However, for finite drive strength only a subset of these states are significantly coupled by the drive or the interactions and the driven system can frequently be treated by considering a subset of all the states. The particular set of states used to describe the system depends on the initial conditions and how the time-dependent Hamiltonian is turned on. For an undriven initial state, one can use the extended basis approach [54], which includes time-periodic states up to a finite number of Fourier components of the drive frequency. In principle, including a large enough Fourier basis provides an accurate description of the Floquet spectrum.

For periodically driven lattices, one can, under the right conditions, further restrict the noninteracting states to a few-band, tight-binding picture. An accurate effective tight-binding description allows for making direct analogies with well-known lattice models, such as the Harper-Hofstadter model of a particle in a lattice with a magnetic field. (The analogy is frequently imperfect, however, due to additional terms in the tight-binding description that are not in the model system.) More importantly, an accurate tight-binding model indicates weak coupling to higher bands and we expect heating to be slow.

1. Tight-binding model

In this section, we derive the tight-binding effective Hamiltonians describing our driven checkerboard lattice. Using a high-frequency Floquet expansion [29], we calculate the total effective Hamiltonian up to second order in the tunneling (which includes Floquet contributions up to first order in the inverse drive frequency). We focus first on the lowest-order term in the expansion (which we refer to as “first order” since it is first order in the tunneling), as it is the term that gives rise to the effective gauge fields responsible for the staggered flux.

Lattice geometry. The bare static lattice unit cell consists of an A and B site, where the B sublattice is offset in energy from the A sublattice by $\hbar\Delta$ (see Fig. 1). The elementary lattice vectors $\mathbf{a}_{1,2}$, the reciprocal lattice vectors $\mathbf{b}_{1,2}$, and the relative positions $d\hat{\delta}_\mu$ of the four nearest neighbors of a given site are

shown in Fig. 1. The unit cell is chosen such that b_i is offset from a_i by $d\hat{\delta}_1$.

First-order effective Hamiltonian. We start by considering only nearest-neighbor tunneling, where the bare real-space Hamiltonian is given by

$$H = - \sum_{i \in A} \sum_{\mu=1}^4 J(a_i^\dagger b_{i+\mu} + a_i b_{i+\mu}^\dagger) - \Delta a_i^\dagger a_i. \quad (\text{A1})$$

The i sum is a 2D sum over unit cells in the lattice, J is the nearest-neighbor tunneling strength, Δ is the staggered energy offset of the B sites, and $b_{i+\mu}$ are the lowering operators for the four B sites that are tunnel coupled to the i th A site along the directions $\hat{\delta}_\mu$ ($\mu = \{1, 2, 3, 4\}$; see Fig. 1).

We consider periodic shaking of the lattice in an elliptical pattern, with inertial force

$$\mathbf{F}(t) = -F[\hat{x} \cos \beta \cos \omega t + \hat{y} \sin \beta \cos(\omega t + \phi_0)]. \quad (\text{A2})$$

Here $\omega = 2\pi/T$ is the radial drive frequency and F is the magnitude of the inertial force due to shaking. The parameters β and ϕ_0 determine the trajectory of the shaking force in the 2D plane, with $\beta = \pi/4$ and $\phi_0 = \pi/2$ corresponding to circular displacement. The driving adds a time-dependent term to H , given by

$$V(t) = - \sum_i \mathbf{F}(t) \cdot (\mathbf{r}_i a_i^\dagger + (\mathbf{r}_i + d\hat{\delta}_1) b_i^\dagger). \quad (\text{A3})$$

The periodic driving term in $H + V(t)$ can be removed by a time-dependent unitary transformation into a basis that compensates for $V(t)$ and shifts the staggered offset Δ by $n\omega$ [29]. The transformation induces time-dependent tunneling constants with different phase lags for the four different tunneling parameters $J_\mu(t)$ associated with tunneling from a given site i to its four nearest neighbors on the other sublattice. The resulting kinetic Hamiltonian has time-dependent tunneling parameters and a shifted sublattice offset of $\delta_n = \Delta - n\omega$,

$$H(t) = \sum_{i \in A} \left[\sum_{\mu=1}^4 (J_\mu(t) a_i^\dagger b_{i+\mu} + \text{H.c.}) - \delta_n (a_i^\dagger a_i) \right], \quad (\text{A4})$$

where

$$J_\mu(t) = -J e^{i\Theta_\mu(t) - in\omega t}. \quad (\text{A5})$$

In Eq. (A4), we have also shifted the overall energy by $\delta_n/2$.

The time-dependent tunneling phases $\Theta_\mu(t)$ are determined from the force $\mathbf{F}(t)$ by time integrating the difference $\mathbf{F} \cdot \Delta \mathbf{r}_i = \mathbf{F} \cdot \hat{\delta}_\mu d$ between each pair of neighboring sites,

$$\begin{aligned} \Theta_\mu(t) &= \frac{-1}{\hbar} \int_0^t \mathbf{F}(t') \cdot d\hat{\delta}_\mu dt' \\ &= \alpha [\cos \phi_\mu \cos \beta \sin \omega t + \sin \phi_\mu \sin \beta \sin(\omega t + \phi_0)]. \end{aligned} \quad (\text{A6})$$

The angles $\phi_\mu = \{\frac{\pi}{4}, \frac{3\pi}{4}, \frac{5\pi}{4}, \frac{7\pi}{4}\}$ are determined by the geometry of the lattice, $\hat{x} \cdot \hat{\delta}_\mu = \cos \phi_\mu$ and $\hat{y} \cdot \hat{\delta}_\mu = \sin \phi_\mu$, and the unitless drive strength is $\alpha = Fd/\hbar\omega$. Simplifying Eq. (A6) gives

$$\Theta_\mu(t) = \alpha A_\mu \sin(\omega t - \varphi_\mu), \quad (\text{A7})$$

where the amplitudes $A_\mu(\beta, \phi_0)$ and phases $\varphi_\mu(\beta, \phi_0)$ of the tunneling modulation depend on the parameters (β, ϕ_0) governing the trajectory. Using the Jacobi-Anger expansion, we can expand $J_\mu(t)$ in Fourier components

$$\begin{aligned} J_\mu(t) &= -J e^{i\alpha A_\mu \sin(\omega t - \varphi_\mu) - i\omega t} \\ &= -J \sum_{s=-\infty}^{\infty} \mathcal{J}_{n+s}(\alpha A_\mu) e^{-i(n+s)\varphi_\mu} e^{ist}. \end{aligned} \quad (\text{A8})$$

Using this expansion for $J_\mu(t)$, $H(t)$ can similarly be expanded in Fourier components

$$H(t) = \sum_{s=-\infty}^{\infty} \tilde{H}_s e^{is\omega t}, \quad (\text{A9})$$

where

$$\begin{aligned} \tilde{H}_s &= -J \sum_{i \in A} \sum_{\mu=1}^4 (\mathcal{J}_{n+s}(\alpha A_\mu) e^{-i(n+s)\varphi_\mu} a_i^\dagger b_{i+\mu} \\ &\quad + \mathcal{J}_{n-s}(\alpha A_\mu) e^{i(n-s)\varphi_\mu} a_i b_{i+\mu}^\dagger). \end{aligned} \quad (\text{A10})$$

For the rest of the discussion of the lowest-order effective Hamiltonian, we will temporarily ignore the offset term $(\delta_n/2)(b_i^\dagger b_i - a_i^\dagger a_i)$.

Deriving the momentum space effective Floquet Hamiltonian from here can proceed in two ways: one can Fourier transform the real-space Hamiltonian (A1) into the momentum basis and then perform the high-frequency Floquet expansion or one can perform the high-frequency expansion in real space first and then Fourier transform the result. While the former is more efficient, the latter leads to expressions for the effective Hamiltonian in real space from which the Peierls phases of the effective gauge field are easy to read out.

The first order (in J) term in the Floquet expansion of (A1) is just the average of $H(t)$, which gives $H^{[1]}(\mathbf{r}) = \tilde{H}_0$:

$$H^{[1]}(\mathbf{r}) = -J \sum_{i \in A} \sum_{\mu=1}^4 (\mathcal{J}_n(\alpha A_\mu) e^{-in\varphi_\mu} a_i^\dagger b_{i+\mu} + \text{H.c.}). \quad (\text{A11})$$

The effective staggered flux Φ is given by the sum of the Peierls phases $n\varphi_\mu$ around a square plaquette, keeping track of the sign changes when traversing opposite to the directed tunneling, $a_i b_{i+\mu}^\dagger$ vs $a_i^\dagger b_{i+\mu}$:

$$\begin{aligned} \Phi &= \pm n \sum_{j=1}^4 (-1)^j \varphi_j \\ &= \mp n(\varphi_1 - \varphi_2 + \varphi_3 - \varphi_4). \end{aligned} \quad (\text{A12})$$

Values of A_μ , φ_μ , and Φ are given in Table I for some example trajectories. For an elliptical trajectory with major axis aligned along \hat{x} or \hat{y} , the staggered flux is continuously variable, $\Phi = \pm 4n\beta$. In particular, for $\beta \simeq \pi/4$ in the $n = 1$ resonant case, the flux can be tuned across the transition at $\Phi = \pi$ [41,42].

We can easily identify the Peierls phases by rearranging the terms in Eq. (A11) from a ‘‘spoke’’ numbering, where tunneling to each of four B sites are counted for every A site, to a ‘‘plaquette’’ accounting, where tunneling along the four bonds of a square are counted for each plaquette, and

TABLE I. Example values of A_μ , φ_μ , and Φ for different trajectories: (a) an elliptical trajectory with major axis aligned along \hat{x} ($\beta < \pi/4$) or \hat{y} ($\beta > \pi/4$); (b) an elliptical trajectory with major axis aligned along $\hat{x} + \hat{y}$; (c) a linear trajectory along a line making an angle β with respect to \hat{x} . It is useful to note that $\cos \phi_\mu = \{1, -1, -1, 1\}/\sqrt{2}$ and $\tan \phi_\mu = \{1, -1, 1, -1\}$.

	Elliptical \hat{x}, \hat{y}	Elliptical $\hat{x} + \hat{y}$	Linear at angle β
	$0 < \beta < \pi/2$ $\phi_0 = \pi/2$	$\beta = \pi/4$ $0 < \phi_0 < \pi/2$	$0 < \beta < \pi/2$ $\phi_0 = 0$
A_μ	$\cos \phi_\mu$	$\sqrt{\frac{1}{2}(1 + \tan \phi_\mu \cos \phi_0)}$	$\cos(\beta - \phi_\mu)$
φ_μ	$\beta \tan \phi_\mu$	$\phi_\mu - \pi/4 + \phi_0/2$	0
Φ	$\pm 4n\beta$	$n\pi$	0

writing out the Hamiltonian explicitly for the elliptical drive case gives

$$\begin{aligned} H^{[1]}(\mathbf{r}) &= -\frac{J}{2} \sum_{\mathcal{P}_j} (e^{-in\beta} a_{j1} b_{j1}^\dagger + e^{-in(\beta-\pi)} a_{j2}^\dagger b_{j1} \\ &\quad + e^{-in(\beta+\pi)} a_{j2} b_{j2}^\dagger + e^{-in\beta} a_{j1}^\dagger b_{j2} + \text{H.c.}). \end{aligned} \quad (\text{A13})$$

Equation (A13) is the Peierls substitution expression for particles on a square lattice with staggered $\Phi = 4n\beta$ flux. (The factor of $1/2$ accounts for overcounting, since the sum is over all plaquettes.)

When dealing with the Fourier transforms of H , it is convenient to define a set of functions,

$$G_s(\mathbf{q}, \alpha A_\mu, \varphi_\mu) = \sum_{\mu=1}^4 \mathcal{J}_s(\alpha A_\mu) e^{-i\mathbf{q} \cdot (\hat{\delta}_\mu - \hat{\delta}_1) - is\varphi_\mu}, \quad (\text{A14})$$

which capture the momentum dependence of the different Fourier transformed terms in the Hamiltonian.

Fourier transforming $H^{[1]}(\mathbf{r})$ [Eq. (A11)] gives the first-order Hamiltonian in momentum space, which is diagonal in \mathbf{q} : $H^{[1]}(\mathbf{q}) = \sum_{\mathbf{q}} (h_1 a_{\mathbf{q}}^\dagger b_{\mathbf{q}} + \text{H.c.})$,

$$h_1 = -J G_n(\mathbf{q}, \alpha A_\mu, \varphi_\mu) \quad (\text{A15})$$

for the near resonant condition $\omega \simeq \Delta/n$, with $n = 1$ or 2 . For each \mathbf{q} in momentum space, h_1 couples the two states corresponding to the A band and B band.

Second-order effective Hamiltonian. As noted in the main text, in the limit $\alpha \rightarrow 0$, the first-order tunneling vanishes as $J\alpha$, while the remaining lowest-order terms scale as J^2 and are nonzero and should therefore be included. The second-order term in the high-frequency Floquet expansion is given by

$$H^{[2]} = \frac{1}{\hbar\omega} \sum_{s=1}^{\infty} \frac{1}{s} [H_s, H_{-s}]. \quad (\text{A16})$$

Evaluating Eq. (A16) in momentum space gives an effective Hamiltonian at this order that is also diagonal in q , $H^{[2]}(\mathbf{q}) = \sum_q h_2 (b_q^\dagger b_q - a_q^\dagger a_q)$, where

$$h_2 = \frac{J^2}{\hbar\omega} \sum_s \frac{1}{s} (|G_{n-s}(\mathbf{q}, \alpha A_\mu, \varphi_\mu)|^2 - |G_{n+s}(\mathbf{q}, \alpha A_\mu, \varphi_\mu)|^2). \quad (\text{A17})$$

Next-nearest-neighbor tunneling Hamiltonian. To be consistent, we also include next-nearest-neighbor tunneling, since it scales as J^2/E_R . These are direct tunneling terms that involve tunneling confined to the same sublattice and depend on additional tight-binding parameters J_a and J_b . In addition, these terms are affected by the modulation at strength 2α :

$$H_{ab}(\mathbf{r}) = \mathcal{J}_0(2\alpha) \sum_{i \in A, B} \sum_{\mu=1}^4 (J_a a_i^\dagger a_{i+2\mu} + J_b b_i^\dagger b_{i+2\mu}), \quad (\text{A18})$$

where the sum over i includes both A and B sites and the index $(i + 2\mu)$ indicates the next-nearest lattice site located at $2\hat{\delta}_\mu$ relative to site A or B on site i . H_{ab} is also diagonal in momentum space, $H_{ab}(\mathbf{q}) = \sum_{\mathbf{q}} h_{ab}(J_a a_{\mathbf{q}}^\dagger a_{\mathbf{q}} + J_b b_{\mathbf{q}}^\dagger b_{\mathbf{q}})$, with

$$h_{ab} = e^{-i\mathbf{q} \cdot (\mathbf{a}_1 + \mathbf{a}_2)} G_0(2\mathbf{q}, 2\alpha, 0). \quad (\text{A19})$$

Combining all these terms together, we have $H = \sum_{\mathbf{q}} H_{\mathbf{q}}$, where

$$H_{\mathbf{q}} = (h_1 a_{\mathbf{q}}^\dagger b_{\mathbf{q}} + \text{H.c.}) + h_2 (a_{\mathbf{q}}^\dagger a_{\mathbf{q}} - b_{\mathbf{q}}^\dagger b_{\mathbf{q}}) + h_{ab}(J_a a_{\mathbf{q}}^\dagger a_{\mathbf{q}} + J_b b_{\mathbf{q}}^\dagger b_{\mathbf{q}}). \quad (\text{A20})$$

In the $(a_{\mathbf{q}}, b_{\mathbf{q}})$ basis, the tight-binding Hamiltonian to second order in J^2 can be written

$$H_{\mathbf{q}} = \begin{pmatrix} -h_2 - J_a h_{ab} & h_1^* \\ h_1 & \delta_n - J_b h_{ab} + h_2 \end{pmatrix}. \quad (\text{A21})$$

The band structure is obtained by diagonalizing this matrix and the energy spectrum is given by

$$\epsilon_{\pm}(\mathbf{q}) = \frac{1}{2} [\delta_n - h_{ab}(J_a + J_b) \pm \sqrt{4|h_1|^2 + [\delta_n + 2h_2 + h_{ab}(J_a - J_b)]^2}]. \quad (\text{A22})$$

2. Extended matrix–full calculation

The periodically driven system can also be treated in the Floquet-Shirley picture, where an extended Hilbert space is introduced. For the details of the approach, we refer the reader to the literature [54–56] and provide here only a brief outline of the calculation. The extended Hilbert space used in this approach is the product of the Hilbert space of the lattice functions and time periodic functions, namely

$$\psi_{nm} = e^{im\omega t} u_n, \quad (\text{A23})$$

where $u_n = u_n(\mathbf{q})$ are the states of the undriven lattice (Bloch states) at a given \mathbf{q} . The spectrum in this picture is determined by the eigenvalues of the “quasimomentum” operator $\hat{Q} \equiv H(t) - i\hbar\partial_t$. For our shaken lattice system, the time-dependent Hamiltonian can be expressed in the frame co-moving with the lattice as

$$H = \frac{|p|^2}{2m} + V_{\text{lat}}(x, y) - \omega[\Delta x \cos(\omega t)p_x + \Delta y \cos(\omega t + \phi)p_y]. \quad (\text{A24})$$

Our single drive frequency results in the matrix element, $H_{\pm 1} = \alpha(p_x + p_y)$, which we numerically calculate. The

quasimomentum operator can be expressed as a block-diagonal matrix with matrix elements

$$\langle n', m' | \hat{Q} | n, m \rangle = \langle n' | H_{m'-m} | n \rangle + \delta_{mm'} \delta_{nn'} m \hbar \omega, \quad (\text{A25})$$

where H_m are the Fourier components of $H(t)$, $H_m = \int_0^T e^{im\omega t} H(t) dt$. For the case of a single drive frequency, the only contributions will arise from $m' - m = 1$, which is $H_{\pm 1}$. The first term in Eq. (A25) couples two static lattice bands, n, n' by the $H_{\pm 1}$ component. The second contribution represents the static Hamiltonian H_0 , offset by integer multiples of the drive frequency.

We numerically calculate the extended basis, which requires truncating the number of Floquet blocks (m), such that there are $2 * m + 1$ blocks in the full extended picture. The energies reported are taken to be the eigenvalues of the operator \hat{Q} .

We note that, for a multiphoton resonance, since there is no direct 2ω component ($H_{\pm 2} = 0$ as defined above), the coupling at resonance comes from an intermediate state and not a direct coupling [57]. In numerically calculating the extended basis picture, if the number of Bloch states are truncated, we find that to recover the tight-binding behavior requires four Bloch states.

APPENDIX B: IMPACT OF GAUGE ON MEASUREMENTS

In order to elucidate the role that a particular experimental gauge plays in the measurements, we consider explicitly two realizations of the ideal, tight-binding model of the same staggered- π flux system: one described by the Hamiltonian in the staggered “symmetric” gauge given here in Eq. (1) and the other in the staggered “Landau” gauge described by Eq. 5 in Ref. [42], based on the proposal in [58]. These two Hamiltonians describe the same “low-energy” physics (up to a rotation and scaling of the spatial basis), where low energy means that any dynamics imposed on the system during a measurement does not excite the atoms outside of the tight-binding basis associated with the lowest dressed band. Under this assumption, the physics of the systems, i.e., the energy spectrum, transport, and response functions, will be identical. For synthetic gauge fields, this assumption can be easily violated, for example, by suddenly turning off the optical lattice, which projects the states onto a range of excited states outside the ground band. The resulting measurement can then be sensitive to the particular experimental realization of the gauge.

Focusing on the single-particle ground states (ignoring interactions), the systems are diagonal in crystal momentum \mathbf{q} . If there are no degeneracies in the spectrum, then the ground states in the different gauges are simply related by an overall phase. If the ground state is degenerate, however, the single-particle wave function can be an arbitrary superposition of the two degenerate solutions, which can be parametrized as in Eq. (3). The solution including mean-field interactions will be the one that minimizes density variations from site to site. For the symmetric gauge used here [Fig. 10(a)], the \mathbf{q} -dependent eigenstates are homogenous and both solutions minimize the interaction. A superposition of the two states [Fig. 10(a)(iii)] has large density modulations, which increases the interaction energy. Conversely, for the Landau gauge [Fig. 10(b)], the

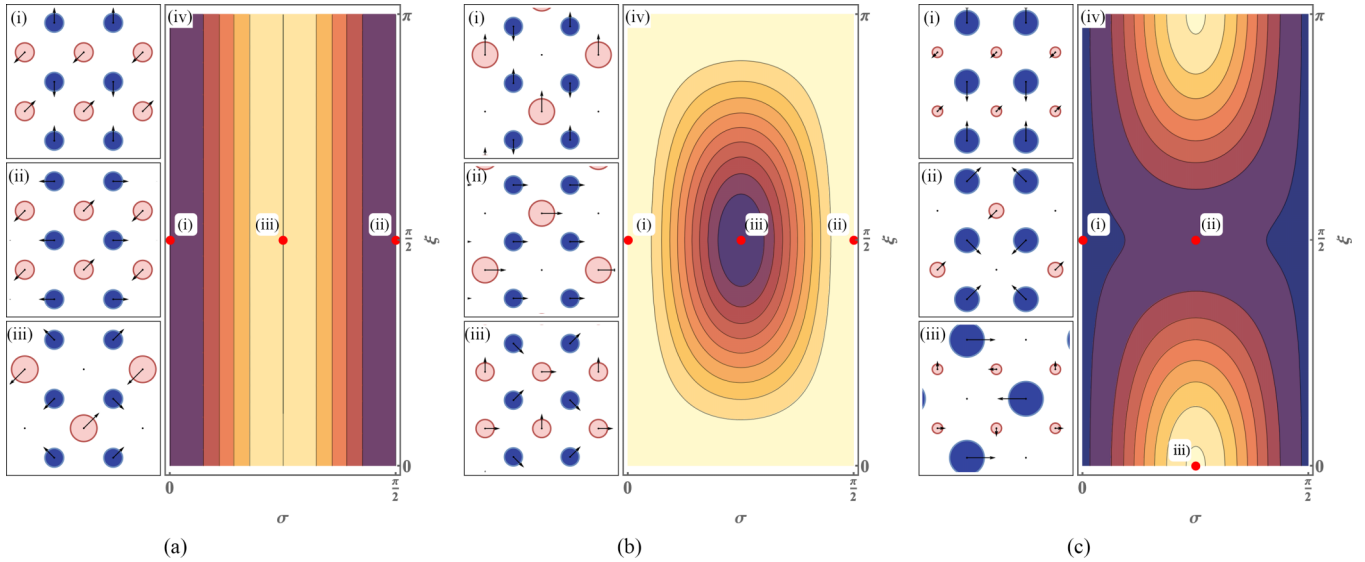


FIG. 10. Gauge dependence of the wave functions. The tight-binding wave function for (a) the staggered symmetric gauge, driven on resonance, (b) the staggered Landau gauge [42], and (c) the staggered symmetric gauge, driven off-resonantly. The Hamiltonian in both the symmetric and Landau gauges is diagonal in momentum $\psi = \psi(\mathbf{q})$, with identical spectra $\epsilon(\mathbf{q})$. The wave functions [shown in subfigures (i), (ii), and (iii)], however, depend on the choice of gauge. The figures show representations of the ideal case tight-binding wave functions, with the same color labeling as Fig. 1 [A (blue); B (red)]. The size of the circles represents the wave-function density at each lattice site, while the arrow indicates the phase. (The Landau gauge implementation is not a checkerboard lattice and the color scheme has no significance for this case; it is included for comparison to the symmetric gauge.) The contour plots in panels (iv) indicate the magnitude of the mean-field energy $U_{\text{int}} \propto |\psi(\sigma, \xi)|^4$ as a function of the superposition of the two \mathbf{q} -dependent eigenstates [main text Eq. (3)]. The labeled red points indicate the particular superposition (σ, ξ) associated with the panels on the left. Blue indicates lower energy. For the detuned symmetric case (c), the energy difference between pure ψ_+ [$(\sigma, \xi) = (\pi/2, 0)$] and a superposition of ψ_+ and ψ_- [$(\sigma, \xi) = (\pi/2, \pi/4)$] becomes small in the large detuning limit.

two q -dependent eigenstates are inhomogeneous and have large interaction energy. A particular superposition $(\sigma, \xi) = (\pi/4, \pi/2)$ minimizes the energy by making the density homogeneous.

As discussed in the main text, in the symmetric gauge we employ here, one would expect the states observed in TOF to fluctuate between the two crystal momenta, which we do not observe. We note that, in the large detuning limit in which we work, the detuning results in a strong staggered density and a particular superposition of the two states with $(\pi/4, \pi/2)$ does not cost too much energy. This small energy could more easily be overcome by an interaction that breaks the phase symmetry that would prefer the $(\sigma, \xi) = (\pi/4, \pi/2)$ state.

APPENDIX C: DATA ANALYSIS

Time-averaged images, shown for example in Fig. 4, were generated by averaging multiple images taken at different snap-off times within the Floquet period, which gives different end phases. Examples of “instantaneous” images of the BEC in a driven lattice are given in Fig. 12 for several end phases, which shows the extent of the micromotion in this system.

In order to determine the crystal momentum populations for the relaxation dynamics shown in Figs. 7–9 of the main text, we take multiple different slices, along either the vertical or horizontal directions, where the width of the slice contains the populations in the diffraction orders selected by the slice.

An example of a horizontal slice targeting the first vertical row of diffraction peaks is shown in Fig. 11. The OD is averaged over the width of the slice and the resulting 1D curve is fit to the sum of Gaussians, one for each expected peak and then an overall central thermal background. The fits have constrained centers and widths, so that the extracted amplitudes are a good estimate of the population. An example curve fit is shown for a specific slice in Fig. 11, where we have a thermal Gaussian and then four additional peaks. In order to analyze this particular shot, there would be four horizontal slices taken, corresponding to the different momentum states that appear in the image. These slices would allow us to reconstruct the total populations in X_{\pm} .

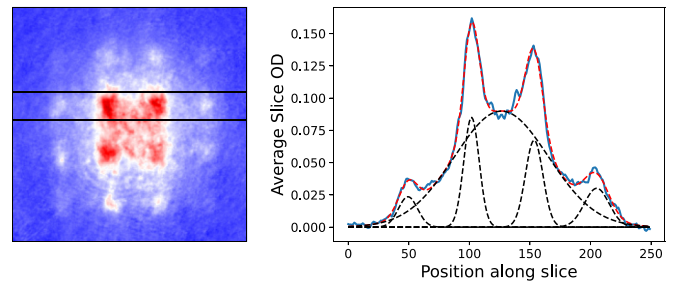


FIG. 11. Left: sample image summed over end phases. The horizontal black lines indicate the slice region as shown as in the right panel. Right: mean slice optical depth of the left image showing an example curve fit of a large central Gaussian and four condensate peaks.

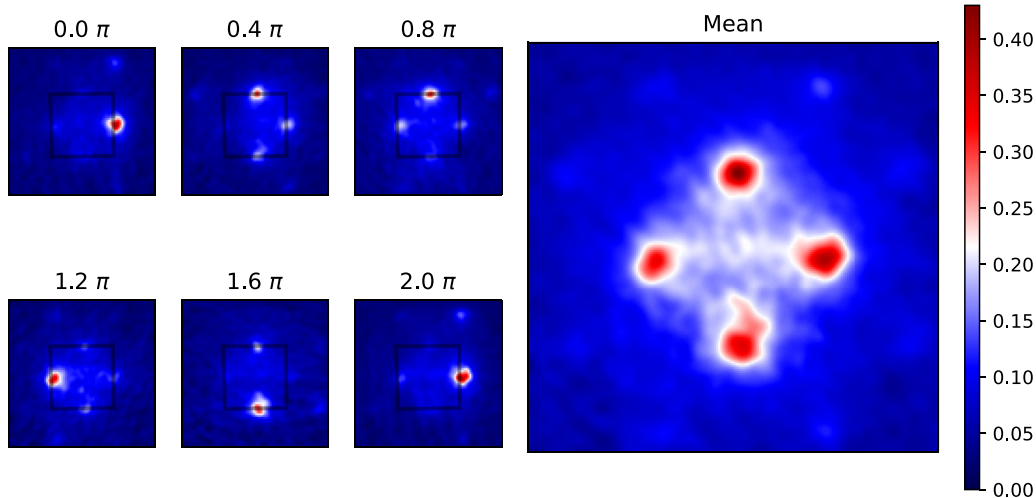


FIG. 12. Micromotion example: TOF absorption images of the atom cloud after suddenly turning off the lattice at different end phases of the drive, as indicated above each image. The micromotion consists of significant periodic modulation of the populations in the different plane-wave components. The mean is scaled by 1.2 to compare on the same color scale.

APPENDIX D: MICROMOTION

Micromotion is the fast, periodic behavior of the state on top of the slow dynamics associated with the effective (static) Floquet Hamiltonian. Although micromotion is typically limited in real space, the actual time-dependent state has strongly modulated occupation of different momentum components. Figure 12 shows an example sequence of state projections

at different phases of the drive period but otherwise identical conditions for the individual phase-averaged image shown in Fig. 4(a). (In order to easily compare the fixed-phase and phase-averaged images visually, here and throughout the paper, we scale the time-averaged images so that the peak optical depth of the average image matches the peak instantaneous optical depth during one period of the instantaneous images contributing to the time-averaged image.)

-
- [1] J. Struck, C. Ölschläger, R. L. Targat, P. Soltan-Panahi, A. Eckardt, M. Lewenstein, P. Windpassinger, and K. Sengstock, Quantum simulation of frustrated classical magnetism in triangular optical lattices, *Science* **333**, 996 (2011).
- [2] J. Struck, M. Weinberg, C. Ölschläger, P. Windpassinger, J. Simonet, K. Sengstock, R. Höppner, P. Hauke, A. Eckardt, M. Lewenstein, and L. Mathey, Engineering Ising-XY spin-models in a triangular lattice using tunable artificial gauge fields, *Nat. Phys.* **9**, 738 (2013).
- [3] L.-C. Ha, L. W. Clark, C. V. Parker, B. M. Anderson, and C. Chin, Roton-maxon excitation spectrum of bose condensates in a shaken optical lattice, *Phys. Rev. Lett.* **114**, 055301 (2015).
- [4] C. V. Parker, L.-C. Ha, and C. Chin, Direct observation of effective ferromagnetic domains of cold atoms in a shaken optical lattice, *Nat. Phys.* **9**, 769 (2013).
- [5] P. Soltan-Panahi, D. S. Löhmann, J. Struck, P. Windpassinger, and K. Sengstock, Quantum phase transition to unconventional multi-orbital superfluidity in optical lattices, *Nat. Phys.* **8**, 71 (2012).
- [6] N. Fläschner, D. Vogel, M. Tarnowski, B. S. Rem, D.-S. Lühmann, M. Heyl, J. C. Budich, L. Mathey, K. Sengstock, and C. Weitenberg, Observation of dynamical vortices after quenches in a system with topology, *Nat. Phys.* **14**, 265 (2018).
- [7] G. Jotzu, M. Messer, R. Desbuquois, M. Lebrat, T. Uehlinger, D. Greif, and T. Esslinger, Experimental realization of the topological haldane model with ultracold fermions, *Nature (London)* **515**, 237 (2014).
- [8] C. A. Bracamontes, J. Maslek, and J. V. Porto, Realization of a floquet-engineered moat band for ultracold atoms, *Phys. Rev. Lett.* **128**, 213401 (2022).
- [9] T. A. Sedrakyán, V. M. Galitski, and A. Kamenev, Statistical transmutation in floquet driven optical lattices, *Phys. Rev. Lett.* **115**, 195301 (2015).
- [10] K. Wintersperger, C. Braun, F. N. Ünal, A. Eckardt, M. D. Liberto, N. Goldman, I. Bloch, and M. Aidelsburger, Realization of an anomalous Floquet topological system with ultracold atoms, *Nat. Phys.* **16**, 1058 (2020).
- [11] L. W. Clark, B. M. Anderson, L. Feng, A. Gaj, K. Levin, and C. Chin, Observation of density-dependent gauge fields in a bose-einstein condensate based on micromotion control in a shaken two-dimensional lattice, *Phys. Rev. Lett.* **121**, 030402 (2018).
- [12] F. Görg, K. Sandholzer, J. Minguzzi, R. Desbuquois, M. Messer, and T. Esslinger, Realization of density-dependent Peierls phases to engineer quantized gauge fields coupled to ultracold matter, *Nat. Phys.* **15**, 1161 (2019).
- [13] C. J. Kennedy, W. C. Burton, W. C. Chung, and W. Ketterle, Observation of bose-einstein condensation in a strong synthetic magnetic field, *Nat. Phys.* **11**, 859 (2015).
- [14] M. Aidelsburger, M. Atala, M. Lohse, J. T. Barreiro, B. Paredes, and I. Bloch, Realization of the hofstadter hamiltonian with ultracold atoms in optical lattices, *Phys. Rev. Lett.* **111**, 185301 (2013).
- [15] H. Miyake, G. A. Siviloglou, C. J. Kennedy, W. C. Burton, and W. Ketterle, Realizing the Harper Hamiltonian with

- laser-assisted tunneling in optical lattices, *Phys. Rev. Lett.* **111**, 185302 (2013).
- [16] T. Bilitewski and N. R. Cooper, Population dynamics in a Floquet realization of the Harper-Hofstadter Hamiltonian, *Phys. Rev. A* **91**, 063611 (2015).
- [17] M. Aidelsburger, M. Lohse, C. Schweizer, M. Atala, J. T. Barreiro, S. Nascimbène, N. R. Cooper, I. Bloch, and N. Goldman, Measuring the Chern number of Hofstadter bands with ultracold bosonic atoms, *Nat. Phys.* **11**, 162 (2015).
- [18] T. Boulier, J. Maslek, M. Bukov, C. Bracamontes, E. Magnan, S. Lellouch, E. Demler, N. Goldman, and J. V. Porto, Parametric heating in a 2D periodically driven bosonic system: Beyond the weakly interacting regime, *Phys. Rev. X* **9**, 011047 (2019).
- [19] K. Wintersperger, M. Bukov, J. Näger, S. Lellouch, E. Demler, U. Schneider, I. Bloch, N. Goldman, and M. Aidelsburger, Parametric instabilities of interacting bosons in periodically driven 1D optical lattices, *Phys. Rev. X* **10**, 011030 (2020).
- [20] M. Reitter, J. Näger, K. Wintersperger, C. Sträter, I. Bloch, A. Eckardt, and U. Schneider, Interaction dependent heating and atom loss in a periodically driven optical lattice, *Phys. Rev. Lett.* **119**, 200402 (2017).
- [21] M. Bukov, M. Heyl, D. A. Huse, and A. Polkovnikov, Heating and many-body resonances in a periodically driven two-band system, *Phys. Rev. B* **93**, 155132 (2016).
- [22] J.-R. Li, B. Shteynas, and W. Ketterle, Floquet heating in interacting atomic gases with an oscillating force, *Phys. Rev. A* **100**, 033406 (2019).
- [23] S. A. Weidinger and M. Knap, Floquet prethermalization and regimes of heating in a periodically driven, interacting quantum system, *Sci. Rep.* **7**, 45382 (2017).
- [24] D. A. Abanin, W. De Roeck, and F. Huveneers, Exponentially slow heating in periodically driven many-body systems, *Phys. Rev. Lett.* **115**, 256803 (2015).
- [25] M. Bukov, S. Gopalakrishnan, M. Knap, and E. Demler, Prethermal Floquet steady states and instabilities in the periodically driven, weakly interacting Bose-Hubbard model, *Phys. Rev. Lett.* **115**, 205301 (2015).
- [26] T. Mori, T. Kuwahara, and K. Saito, Rigorous bound on energy absorption and generic relaxation in periodically driven quantum systems, *Phys. Rev. Lett.* **116**, 120401 (2016).
- [27] D. A. Abanin, W. De Roeck, W. W. Ho, and F. Huveneers, Effective Hamiltonians, prethermalization, and slow energy absorption in periodically driven many-body systems, *Phys. Rev. B* **95**, 014112 (2017).
- [28] A. Rubio-Abadal, M. Ippoliti, S. Hollerith, D. Wei, J. Rui, S. L. Sondhi, V. Khemani, C. Gross, and I. Bloch, Floquet prethermalization in a Bose-Hubbard system, *Phys. Rev. X* **10**, 021044 (2020).
- [29] M. Račiūnas, G. Žlabys, A. Eckardt, and E. Anisimovas, Modified interactions in a Floquet topological system on a square lattice and their impact on a bosonic fractional Chern insulator state, *Phys. Rev. A* **93**, 043618 (2016).
- [30] P. Hauke, O. Tieleman, A. Celi, C. Ölschläger, J. Simonet, J. Struck, M. Weinberg, P. Windpassinger, K. Sengstock, M. Lewenstein, and A. Eckardt, Non-abelian gauge fields and topological insulators in shaken optical lattices, *Phys. Rev. Lett.* **109**, 145301 (2012).
- [31] C. E. Creffield, G. Pieplow, F. Sols, and N. Goldman, Realization of uniform synthetic magnetic fields by periodically shaking an optical square lattice, *New J. Phys.* **18**, 093013 (2016).
- [32] H. Lignier, C. Sias, D. Ciampini, Y. Singh, A. Zenesini, O. Morsch, and E. Arimondo, Dynamical control of matter-wave tunneling in periodic potentials, *Phys. Rev. Lett.* **99**, 220403 (2007).
- [33] C. J. Fujiwara, K. Singh, Z. A. Geiger, R. Senaratne, S. V. Rajagopal, M. Lipatov, and D. M. Weld, Transport in Floquet-Bloch bands, *Phys. Rev. Lett.* **122**, 010402 (2019).
- [34] K.-X. Yao, Z. Zhang, and C. Chin, Domain-wall dynamics in Bose-Einstein condensates with synthetic gauge fields, *Nature (London)* **602**, 68 (2022).
- [35] K. Sandholzer, A.-S. Walter, J. Minguzzi, Z. Zhu, K. Viebahn, and T. Esslinger, Floquet engineering of individual band gaps in an optical lattice using a two-tone drive, *Phys. Rev. Res.* **4**, 013056 (2022).
- [36] B. K. Stuhl, H.-I. Lu, L. M. Ayccock, D. Genkina, and I. B. Spielman, Visualizing edge states with an atomic Bose gas in the quantum Hall regime, *Science* **349**, 1514 (2015).
- [37] M. Mancini, G. Pagano, G. Cappellini, L. Livi, M. Rider, J. Catani, C. Sias, P. Zoller, M. Inguscio, M. Dalmonte, and L. Fallani, Observation of chiral edge states with neutral fermions in synthetic Hall ribbons, *Science* **349**, 1510 (2015).
- [38] A. Celi, P. Massignan, J. Ruseckas, N. Goldman, I. B. Spielman, G. Juzeliūnas, and M. Lewenstein, Synthetic gauge fields in synthetic dimensions, *Phys. Rev. Lett.* **112**, 043001 (2014).
- [39] G. Wirth, M. Olschlager, and A. Hemmerich, Evidence for orbital superfluidity in the *P*-band of a bipartite optical square lattice, *Nat. Phys.* **7**, 147 (2011).
- [40] T. Kock, M. Ölschläger, A. Ewerbeck, W.-M. Huang, L. Mathey, and A. Hemmerich, Observing chiral superfluid order by matter-wave interference, *Phys. Rev. Lett.* **114**, 115301 (2015).
- [41] L.-K. Lim, C. M. Smith, and A. Hemmerich, Staggered-vortex superfluid of ultracold bosons in an optical lattice, *Phys. Rev. Lett.* **100**, 130402 (2008).
- [42] G. Möller and N. R. Cooper, Condensed ground states of frustrated Bose-Hubbard models, *Phys. Rev. A* **82**, 063625 (2010).
- [43] L.-K. Lim, A. Hemmerich, and C. M. Smith, Artificial staggered magnetic field for ultracold atoms in optical lattices, *Phys. Rev. A* **81**, 023404 (2010).
- [44] H. Fu, A. Glatz, F. Setiawan, K.-X. Yao, Z. Zhang, C. Chin, and K. Levin, Dynamical preparation of an atomic condensate in a Hofstadter band, *Phys. Rev. A* **105**, 043301 (2022).
- [45] Y. J. Lin, R. L. Compton, K. Jimenez-Garcia, W. D. Phillips, J. V. Porto, and I. B. Spielman, A synthetic electric force acting on neutral atoms, *Nat. Phys.* **7**, 531 (2011).
- [46] S. Powell, R. Barnett, R. Sensarma, and S. Das Sarma, Bogoliubov theory of interacting bosons on a lattice in a synthetic magnetic field, *Phys. Rev. A* **83**, 013612 (2011).
- [47] J. Sebby-Strabley, M. Anderlini, P. S. Jessen, and J. V. Porto, Lattice of double wells for manipulating pairs of cold atoms, *Phys. Rev. A* **73**, 033605 (2006).
- [48] S. B. Koller, E. A. Goldschmidt, R. C. Brown, R. Wyllie, R. M. Wilson, and J. V. Porto, Nonlinear looped band structure of Bose-Einstein condensates in an optical lattice, *Phys. Rev. A* **94**, 063634 (2016).
- [49] E. Magnan, J. Maslek, C. Bracamontes, A. Restelli, T. Boulier, and J. V. Porto, A low-steering piezo-driven mirror, *Rev. Sci. Instrum.* **89**, 073110 (2018).

- [50] M. Aidelsburger, M. Atala, S. Nascimbène, S. Trotzky, Y.-A. Chen, and I. Bloch, Experimental realization of strong effective magnetic fields in an optical lattice, *Phys. Rev. Lett.* **107**, 255301 (2011).
- [51] M. Ölschläger, G. Wirth, and A. Hemmerich, Unconventional superfluid order in the F band of a bipartite optical square lattice, *Phys. Rev. Lett.* **106**, 015302 (2011).
- [52] Y.-J. Lin, K. Jiménez-García, and I. B. Spielman, Spin-orbit-coupled Bose–Einstein condensates, *Nature (London)* **471**, 83 (2011).
- [53] A. Eckardt, Colloquium: Atomic quantum gases in periodically driven optical lattices, *Rev. Mod. Phys.* **89**, 011004 (2017).
- [54] A. Eckardt and E. Anisimovas, High-frequency approximation for periodically driven quantum systems from a Floquet-space perspective, *New J. Phys.* **17**, 093039 (2015).
- [55] J. H. Shirley, Solution of the Schrödinger equation with a Hamiltonian periodic in time, *Phys. Rev.* **138**, B979 (1965).
- [56] M. Holthaus, Floquet engineering with quasienergy bands of periodically driven optical lattices, *J. Phys. B: At., Mol., Opt. Phys.* **49**, 013001 (2016).
- [57] M. Weinberg, C. Ölschläger, C. Sträter, S. Prella, A. Eckardt, K. Sengstock, and J. Simonet, Multiphoton interband excitations of quantum gases in driven optical lattices, *Phys. Rev. A* **92**, 043621 (2015).
- [58] F. Gerbier and J. Dalibard, Gauge fields for ultracold atoms in optical superlattices, *New J. Phys.* **12**, 033007 (2010).